REPORT DOCUMENTATION PAGE

Public reporting burden for this collection of information is estimated to average 1 hour per response, including the time for reviewing instructions, searching existing data sources, gathering and maintaining the data needed, and completing and reviewing the collection of information. Send comments regarding this burden estimate or any other aspect of this collection of information, including suggestions for reducing this burden, to Washington Headquarters Services, Directorate for Information Operations and Reports, 1215 Jefferson Davis Highway, Suite 1204, Arlington, VA 22202-4302, and to the Office of Management and Budget, Paperwork Reduction Project (0704-0188), Washington, DC 20503.

1. AGENCY USE ONLY (Leave blank)	2. REPORT DATE	3. REPORT TYPE AND DATES COVERED
		Final

4. TITLE AND SUBTITLE Compressible Flow Turbulence Simulation & Modeling via ATD

5. FUNDING NUMBERS F49620-92-J-0488

6. AUTHOR(S) Jim McDonough

7. PERFORMING ORGANIZATION NAME(S) AND ADDRESS(ES) University of Kentucky

AFOSR-TR-96
0146

9. SPONSORING/MONITORING AGENCY NAME(S) AND ADDRESS(ES)

Air Force Office Of Scientific Research
Aerospace & Materials Sciences Directorate
110 Duncan Avenue, Suite B-115
Bolling AFB DC 20332-0001
Dr. Len Sakell

NA

3484 EI

10. SPONSORING/MONITORING AGENCY REPORT NUMBER

11. SUPPLEMENTARY NOTES

12a. DISTRIBUTION/AVAILABILITY STATEMENT

APPROVED FOR PUBLIC RELEASE
DISTRIBUTION IS UNLIMITED

12b. DISTRIBUTION CODE

19960404 054

13. ABSTRACT (Maximum 200 words)

This report documents the research conducted under AFOSR Grant F49620-92-J-0488, "Compressible Flow Turbulence Simulation and Modeling via Additive Turbulent Decomposition," during the period 09/01/92-11/30/95.

We begin by noting that four graduate students have been supported during the course of this grant: Mr. D. Denger, Ms. S. Flynn, Mr. E. C. Hylin and Mr. D. C. Weatherly. The first two chose to leave the project before the end of the first year; Ms. Flynn received her M.S. in Mechanical Engineering shortly thereafter, and Mr. Denger is expected to receive his Ph.D. in Mechanical Engineering at least by the end of Summer 1996. Both of the remaining two students, Mr. Hylin and Mr. Weatherly, anticipate completing their Ph.D.s in Mechanical Engineering during the current semester, Spring '96. Thus, the grant will have aided, very crucially in the latter two cases, in producing four advanced engineering degrees.

14. SUBJECT TERMS Additive Turbulent Decomposition

15. NUMBER OF PAGES

16. PRICE CODE

17. SECURITY CLASSIFICATION OF REPORT	18. SECURITY CLASSIFICATION OF THIS PAGE	19. SECURITY CLASSIFICATION OF ABSTRACT	20. LIMITATION OF ABSTRACT

NSN 7540-01-280-5500

DTIC QUALITY INSPECTED 1

Standard Form 298 (Rev. 2-89)

COMPRESSIBLE FLOW TURBULENCE
SIMULATION AND MODELING
VIA ADDITIVE TURBULENT
DECOMPOSITION

(Final Report: 1992–1995)

AFOSR Grant F49620–92–J–0488

Principal Investigator
J. M. McDonough

Graduate Students
E. C. Hylin
D. C. Weatherly

31 January 1996

Contents

1 Introduction

This report documents the research conducted under AFOSR Grant F49620–92–J–0488, "Compressible Flow Turbulence Simulation and Modeling via Additive Turbulent Decomposition," during the period 09/01/92–11/30/95.

We begin by noting that four graduate students have been supported during the course of this grant: Mr. D. Denger, Ms. S. Flynn, Mr. E. C. Hylin and Mr. D. C. Weatherly. The first two chose to leave the project before the end of the first year; Ms. Flynn received her M.S. in Mechanical Engineering shortly thereafter, and Mr. Denger is expected to receive his Ph.D. in Mechanical Engineering at least by the end of Summer 1996. Both of the remaining two students, Mr. Hylin and Mr. Weatherly, anticipate completing their Ph.D.s in Mechanical Engineering during the current semester, Spring '96. Thus, the grant will have aided, very crucially in the latter two cases, in producing four advanced engineering degrees.

The work to be reported here deviates somewhat from that originally proposed, at least in part due to our evolving understanding of the additive turbulent decomposition (ATD) formalism. In particular, it was originally proposed to study both the simulation and modeling aspects of ATD applied to compressible flow. However, by the beginning of the second year of the project, parallelization studies of ATD being conducted under NSF sponsorship were beginning to show that while predicted parallel speedups were indeed achievable, the number of processors needed for high-Re engineering calculations far exceeded that likely to be available in the near term, so the direct simulation version of ATD is not likely to be widely useful very soon. At the same time, and in part motivated by these findings, we began incompressible flow studies employing ATD as the foundation for a new class of turbulence modeling techniques. Initial results were extremely promising, so we pursued this approach for both compressible and incompressible flow.

The basic idea underlying this approach has been reported in earlier progress reports for this and other grants, and it will be discussed at some length in the sequel. It consists of solving unaveraged equations for the large-scale quantities—these equations containing both large- and small- (and any appropriate intermediate-) scale variables—and modeling everything else using nonlinear algebraic maps. This approach is extremely straightforward. It greatly reduces the number of quantities that must be modeled, compared with Reynolds-averaged approaches, and it allows time-accurate calculations including interactions between turbulence and other physical phenomena.

It is crucial to recognize that it is the fluctuating primitive variables themselves, and *not* their correlations, that are being modeled. Figure 1 depicts some typical results for 2-D incompressible flow over a backward-facing step at $Re = 1.32 \times 10^5$. Parts (a) and (b) show instantaneous streamlines of the complete and small-scale velocity fields respectively. Of particular interest in part (a) of the figure are the secondary vortices at the downstream end of the main vortex. It is important to
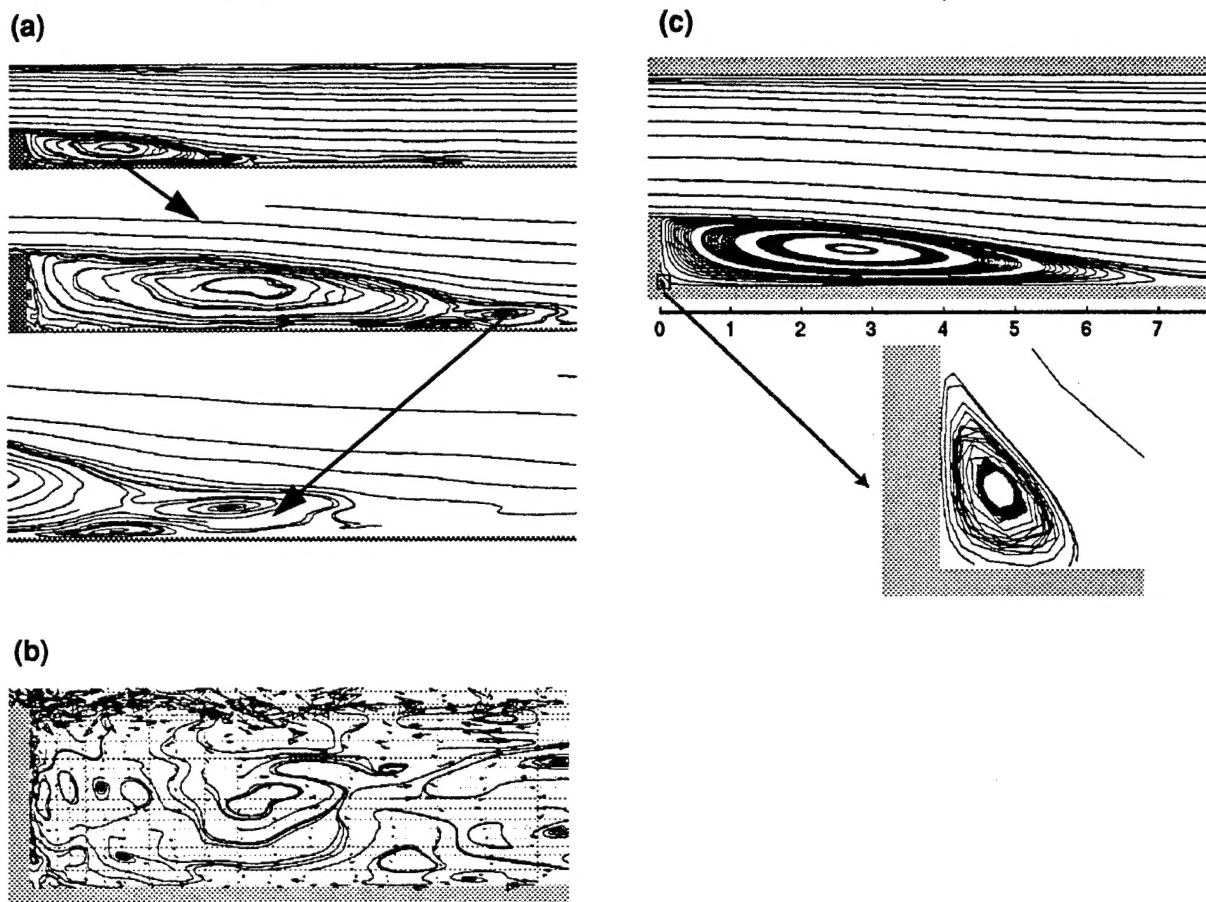
Figure 1: Modeled flow over a 2-D backward-facing step.

note that these are transient, and that they do not occur if the small-scale model is omitted. Part (b) of the figure indicates that the instantaneous mass-conserved small-scale velocity exhibits a wide range of length scales, at least some of which interact with the large-scale motion.

Finally, in part (c) we display the time-averaged behavior. The salient points to note are: i) the main vortex is smooth and of a length comparable to experimental observations, and ii) a secondary vortex in the lower corner of the step has been resolved, even on the fairly coarse (but stretched) 61×46 grid. It is also worth mentioning that Reynolds stresses and turbulent kinetic energy are in reasonable agreement with experimental data.

The run time required for this simulation (without parallelization) is within a factor of 1.5 of that required by the standard k–ϵ model on the same grid. Fairly straightforward parallelization would reduce this considerably, even if only relatively few processors are employed (as few as two).

In the following sections of this report we will present the chaotic-map modeling procedure in fair detail (a complete treatment is available in Hylin & Mc-Donough [2]), along with discussions concerning 2-D and 3-D implementations for the GASP compressible code. Computed results for a $M_\infty = 2.85$ flow over a compression ramp will be presented for the 2-D case, and initial 3-D results associated with vortex-stimulated flows will also be given. Completion of the 3-D incompressible and 3-D compressible versions of the ATD/chaotic-map modeling formalisms is the remaining Ph.D. dissertation research requirement for Mr. Hylin and Mr. Weatherly respectively.

2 Review

Since September of 1994, we have continued to refine our idea of a new class of turbulence models, which model fluctuations in the primitive variables instead of modeling statistically averaged quantities such as the Reynolds stress or the turbulent kinetic energy and dissipation. By taking this approach, the subgrid-scale stresses generated by our models are guaranteed to be physically realizable—unlike many classical turbulence models, ours will never generate a negative kinetic energy. In fact, it has proven possible to construct models that *by design* duplicate many features of physical turbulence at small scales.

Our models are enabled by several fundamental ideas. First, to decompose the conserved variables in the equations of fluid motion into large-scale and small-scale components, and then to decompose the equations themselves into two coupled sets of equations governing the evolution of these components. Second, to replace the evolution equations for the small-scale quantities with stochastic small-scale fields; that is, to create stochastic models for the small-scale fluctuations in the conserved variables, and use these models to generate the spatio-temporal fields associated with these quantities—for example, the small-scale velocity field. Third, to generate the necessary stochastic variables via chaotic maps, and to tailor these

so as to mimic as closely as possible the dynamical and statistical behavior of a physical small-scale flow. Fourth, to scale the amplitude of the small-scale fluctuations to match the turbulent spectra, especially the spectrum for the turbulent kinetic energy. And fifth, to use local samples of the large-scale flow structure to estimate the local anisotropy and one-point velocity correlations for the subgrid-scale flow.

In our previous report, certain areas of our models were identified as being most in need of refinement. These included the decomposition of the governing equations, the relation between large-scale flow parameters and the dynamical parameter(s) governing our chaotic maps, the scaling in compressible flows of the energy and density fluctuations, and the form of the chaotic maps as it relates to the statistical properties of real turbulence. We have made significant progress in two of these areas: the decomposition of the equations and the form of the chaotic maps. Refinement of the energy and density fluctuations still awaits better turbulent spectra for these quantities, while an improved relation between the flow and map parameters likely depends on progress in dynamical systems theory.

3 Decomposition

Previously we had split the large-scale and small-scale equations on something of an *ad hoc* basis, relying on heuristic arguments that the large-scale and small-scale equations should have the same form, and that they should take the form of transport equations for the large-scale and small-scale quantities. There was some evidence, however, that the splitting could be made more mathematically rigorous if it was defined in terms of projections, such that the large-scale equation was derived via a projection onto the large-scale basis, and the small-scale equation derived via a complementary projection. We have succeeded in the effort to define such a splitting, which will now be described.

3.1 Projection Operators for the Large and Small Scales

In additive turbulent decomposition, as in large-eddy simulation, the first step is to split the dependent variables into large-scale and small-scale components by means of a spatial filter. If for some set of basis functions this filter is spectrally sharp, then the large-scale components represent the first few terms in the corresponding functional expansion for the variables, while the small-scale components represent the remainder of the expansion. Thus if the velocity u may be expressed as the weighted sum of a series of basis functions:

$$u \equiv \sum_{\kappa} \hat{u}_{\kappa} \phi(\kappa \cdot x), \tag{1}$$

where $\phi(\kappa \cdot x)$ is the basis function for the wavenumber κ, operating on the position vector x, while $\hat{u}_{\kappa}$ is the corresponding weight; then the large-scale velocity may

4

be expressed as

$$u_L \equiv \sum_{|\boldsymbol{\kappa}| \leq N} \hat{u}_{\boldsymbol{\kappa}} \phi(\boldsymbol{\kappa}{\cdot}\boldsymbol{x}) \equiv \mathbb{P}_L(\boldsymbol{u}), \qquad (2)$$

while the small-scale velocity is expressed as

$$u_S \equiv \sum_{|\boldsymbol{\kappa}| > N} \hat{u}_{\boldsymbol{\kappa}} \phi(\boldsymbol{\kappa}{\cdot}\boldsymbol{x}) = (I - \mathbb{P}_L)(\boldsymbol{u}) \equiv \mathbb{P}_S(\boldsymbol{u}). \qquad (3)$$

Equations (2) and (3) define $\mathbb{P}_L$ as the *projection operator* for the large-scale basis, and $\mathbb{P}_S$ as the complementary projection operator for the small-scale basis.

3.2 The Large- and Small-Scale Equations

If the projection operators $\mathbb{P}_L$ and $\mathbb{P}_S$ are applied to the incompressible Navier–Stokes equations, then since the time derivative operator commutes with the spatial projectors, one obtains differential equations for the large-scale and small-scale velocities:

$$\frac{\partial u_L}{\partial t} + \mathbb{P}_L \left[\boldsymbol{\nabla}{\cdot}(\boldsymbol{u}_L \boldsymbol{u}_L) + \boldsymbol{\nabla}{\cdot}(\boldsymbol{u}_S \boldsymbol{u}_L) + \boldsymbol{\nabla}{\cdot}(\boldsymbol{u}_L \boldsymbol{u}_S) + \boldsymbol{\nabla}{\cdot}(\boldsymbol{u}_S \boldsymbol{u}_S) \right]$$
$$= -\mathbb{P}_L(\boldsymbol{\nabla} P) + \nu \mathbb{P}_L \Delta(\boldsymbol{u}_L + \boldsymbol{u}_S), \quad (4)$$

$$\frac{\partial u_S}{\partial t} + \mathbb{P}_S \left[\boldsymbol{\nabla}{\cdot}(\boldsymbol{u}_L \boldsymbol{u}_L) + \boldsymbol{\nabla}{\cdot}(\boldsymbol{u}_S \boldsymbol{u}_L) + \boldsymbol{\nabla}{\cdot}(\boldsymbol{u}_L \boldsymbol{u}_S) + \boldsymbol{\nabla}{\cdot}(\boldsymbol{u}_S \boldsymbol{u}_S) \right]$$
$$= -\mathbb{P}_S(\boldsymbol{\nabla} P) + \nu \mathbb{P}_S \Delta(\boldsymbol{u}_L + \boldsymbol{u}_S), \quad (5)$$

$$\mathbb{P}_L \left[\boldsymbol{\nabla}{\cdot}(\boldsymbol{u}_L + \boldsymbol{u}_S) \right] = 0, \qquad (6)$$

and

$$\mathbb{P}_S \left[\boldsymbol{\nabla}{\cdot}(\boldsymbol{u}_L + \boldsymbol{u}_S) \right] = 0. \qquad (7)$$

Defined in this way, this *coupled system* of equations for $\boldsymbol{u}_L$ and $\boldsymbol{u}_S$ is equivalent to the Navier–Stokes equations. Because the projection and convolution operators do not commute, there is necessarily coupling through the advective terms, but in general there is coupling through the diffusive terms as well.

An exception occurs when the Fourier functions are used for the basis functions ϕ. Then the projections commute with spatial differentiation; the diffusive terms uncouple, as do (6) and (7), so the incompressible continuity equation holds separately on the large and small scales. Also in this case a large-scale and a small-scale pressure may be defined straightforwardly through corresponding pressure Poisson equations:

$$\Delta P_L = -\boldsymbol{\nabla}{\cdot} \left\{ \boldsymbol{\nabla}{\cdot} \left[\mathbb{P}_L(\boldsymbol{u}_L \boldsymbol{u}_L) + \mathbb{P}_L(\boldsymbol{u}_S \boldsymbol{u}_L) + \mathbb{P}_L(\boldsymbol{u}_L \boldsymbol{u}_S) + \mathbb{P}_L(\boldsymbol{u}_S \boldsymbol{u}_S) \right] \right\}, \quad (8)$$

and

$$\Delta P_S = -\nabla \cdot \{\nabla \cdot [\mathbb{P}_S(u_L u_L) + \mathbb{P}_S(u_S u_L) + \mathbb{P}_S(u_L u_S) + \mathbb{P}_S(u_S u_S)]\}. \quad (9)$$

Certain other bases—the Chebyshev and Legendre polynomials, for example—permit a partial simplification of the large-scale and small-scale equations. However the small-scale velocity always influences the large-scale advection, as the large-scale velocity influences the small-scale advection, and consequently the large-scale and small-scale velocities must (in principle) be solved for simultaneously.

4 Stochastic Small-Scale Fields

Before proceeding with the description of our subgrid-scale model, let us consider some features of a stochastic small-scale field. If the large-scale velocity field is defined, for example, on a finite-difference grid with a spacing of h (the coarse grid), the small-scale field may be defined on a grid with a spacing of $h/2$ (the fine grid). Since in this case the fine grid includes the points of the coarse grid, the basis defined by the fine grid overlaps—indeed, it *includes*—that defined by the coarse grid. However, what distinguishes the velocity fields we shall define on the fine grid as being *stochastic small-scale fields* are the following features:

1. A stochastic variable or variables will be used to assign a value to each gridpoint.

2. These values will be updated at time intervals determined in part by the grid spacing, and commensurate with the expected turnover time for subgrid-scale eddies.

3. The maximum magnitude of these values will be a small fraction of the maximum large-scale velocity.

4. Over distances larger than a small multiple of the grid spacing, these values will be *uncorrelated.*

5. The large-scale velocity field will be filtered to reduce or eliminate fluctuations occuring on a scale *smaller* than a small multiple of the grid spacing.

As a consequence of these features, the large-scale and small-scale velocity fields evolve on different spatial and temporal scales. And while transitory large-scale structures may appear in the small-scale field, they will endure only a small fraction of the characteristic large-scale time, and will have an amplitude that is only a small fraction of the characteristic large-scale velocity. Nonetheless, it is such transitory structures that will provide the means for the advective coupling of the large and small scales.

6

5 Subgrid-Scale Model

The idea we are following is to create a stochastic small-scale field by defining a fluctuating value at each point in, say, a finite-difference grid. (We have also applied this technique to a finite-volume discretization.) From a mathematical viewpoint, each of these fluctuating values can generally be resolved into the sum of several contributing terms, each of which takes the form of an amplitude coefficient multiplying a normalized stochastic variable. Our analysis, however, proceeds from a physical viewpoint in which each fluctuating value is produced by a combination of physical effects, which are added or multiplied together as appropriate. We shall now consider these components one at a time.

5.1 Basic Forms and Amplitudes

For compressible flow, the model for the subgrid-scale velocity fluctuations $\boldsymbol{w}_S$ takes the form

$$\boldsymbol{w}_S = C_u w_* Re_h^{\frac{1}{6}}(\boldsymbol{\zeta} \circ \boldsymbol{M}). \tag{10}$$

Here $\boldsymbol{w}_S$ is the subgrid-scale velocity weighted by the square-root of the density, while on the right-hand side the first three terms together specify the amplitude of the fluctuations, the fourth term, $\boldsymbol{\zeta}$, is a vector of anisotropy coefficients, and the fifth term, $\boldsymbol{M}$ is a vector of values from the chaotic maps that generate the normalized stochastic variables. These last two terms are multiplied together in a vector Hadamard product, defined for two vectors and a unit vector $\hat{\boldsymbol{\imath}}$ according to:

$$(\boldsymbol{\zeta} \circ \boldsymbol{M}) \cdot \hat{\boldsymbol{\imath}} \equiv (\boldsymbol{\zeta} \cdot \hat{\boldsymbol{\imath}})(\boldsymbol{M} \cdot \hat{\boldsymbol{\imath}}). \tag{11}$$

For incompressible flow velocities a similar expression is used, in which a quantity u_*, a friction velocity, replaces the quantity w_*, the friction velocity weighted by the square-root of the density, and the result is a pure velocity, $\boldsymbol{u}_S$.

The terms in the expression for the velocity fluctuations have the following meanings. Re_h is a small-scale Reynolds number,

$$Re_h \equiv \frac{h^2 \|\nabla \boldsymbol{u}\|}{\nu}, \tag{12}$$

where h is the local grid-cell characteristic length (which in generalized coordinates we take to be the matrix 2-norm of the inverse of the coordinate transformation matrix), ν is the (molecular) kinematic viscosity, and $\|\nabla \boldsymbol{u}\|$ denotes the 2-norm of the Jacobian matrix (with respect to spatial coordinates) of the large-scale velocity vector. As mentioned above, w_* is a density-weighted friction velocity and is defined according to:

$$w_* \equiv \rho^{\frac{1}{2}}(\nu \|\nabla \boldsymbol{u}\|)^{\frac{1}{2}} \equiv \rho^{\frac{1}{2}} u_*. \tag{13}$$

7

C_u is an amplitude pre-factor that in general is a function of the small-scale Reynolds number Re_h and the Taylor microscale Reynolds number Re_λ, but in the inertial subrange assumes a nearly constant value: $C_u \approx 0.877$.

The amplitude factor $(C_u w_* Re_h^{\frac{1}{6}})$ determined for the velocity fluctuations is in accordance with Komogorov's second similarity hypothesis [6]; this hypothesis implies that over a distance h in the inertial subrange, turbulent velocity fluctuations Δu should scale as

$$\Delta u \sim (h\epsilon)^{\frac{1}{3}}, \tag{14}$$

where ϵ is the energy dissipation.

In the compressible case, we compute additionally the density and energy fluctuations. The former is given by

$$\rho_S = \rho_L C_\rho C_u \left(\frac{h}{L}\right) Re_h^{-\frac{1}{3}} M_\rho. \tag{15}$$

Here M_ρ is an instance of the normalized stochastic variable, while the preceding terms together constitute the amplitude factor. Several of these terms have been previously defined; of the others, ρ_L is the large-scale density, L is a large-scale characteristic length, and C_ρ is a possible $O(1)$ coefficient. This amplitude factor was derived by assuming that the ratio of the small-scale density fluctuations to the large-scale density is of the same order as the ratio of the small-scale velocity fluctuations to the large-scale velocity. That is,

$$\frac{\rho_S}{\rho_L} \sim \frac{\|\boldsymbol{u}_S\|}{\|\boldsymbol{u}_L\|}. \tag{16}$$

Rather than use such an *ad hoc* assumption, we would prefer to obtain the density amplitude function in the same way we obtained the velocity amplitude function: by matching an assumed power-law scaling function to an experimental and/or theoretical spectrum. Unfortunately, as far as we know, such a spectrum has yet to be determined. At least, the assumption we have adopted does not appear to lead to any obvious contradictions.

For the energy amplitude functions, the basic assumption is that the small-scale internal and kinetic energy fluctuations are of the same order; that is,

$$\frac{1}{2}(\rho\boldsymbol{u})_S \cdot \boldsymbol{u} \sim (\rho e)_S \sim (\rho E)_S, \tag{17}$$

where e is the internal energy and E is the total energy. This assumption is supported by some work by Kida & Orszag [5]. However, we expect there to be *two* sources of small-scale kinetic energy fluctuations: a purely small-scale term and a cross-term involving both the large-scale and small-scale velocities. Accordingly, the expression we assume to model the small-scale energy fluctuations in total energy is:

$$(\rho E)_S = A_{EC} M_C M_S + A_{ES} M_S^2, \tag{18}$$

8

where A_{EC} and A_{ES} are the amplitude factors for the cross term and purely small-scale term respectively, while M_C and M_S are two different *independent* instances of the normalized stochastic variable. The amplitude factors are given by:

$$A_{ES} = C_{ES} C_u^2 w_*^2 Re_h^{\frac{1}{3}}, \tag{19}$$

$$A_{EC} = C_{EC} C_u w_*^2 Re_h^{\frac{2}{3}}. \tag{20}$$

On the basis of the assumption that the fluctuations in the kinetic and internal energy should be of the same order, we expect that $\frac{3}{2} \lesssim C_{ES} \lesssim 3$, and $C_{ES} \lesssim C_{EC} \lesssim 2C_{ES}$. As in the case of the density fluctuations we should prefer to base these amplitudes on an experimental or theoretical spectrum, but such seem to be lacking. The experimental determination of spectra for turbulent density and internal-energy fluctuations in compressible flow is much needed.

5.2 Anisotropy

While the amplitude of the small-scale density fluctuations can (presumably) be expressed by a single coefficient, and the amplitude of the energy fluctuations by one coefficient on each of the two contributing terms, the amplitude of the small-scale velocity fluctuations must, in general, be expressed by a vector of coefficients, because the velocity is a vector function. We have chosen to express this amplitude vector as the product of an amplitude coefficient and a vector s of anisotropy coefficients.

There are two potential sources of anisotropy, one arising from the physics and the other from the numerics of the flow. The former is simply the anisotropy of the physical flow structure, which is manifest in a difference between the magnitudes of the three components of the turbulent fluctuations in the physical velocity; the latter is due to whatever anisotropy there is in the grid spacing. Both impact the amplitudes that should be specified for the velocity fluctuations.

In modelling the anisotropies inherent in the flow, we hypothesize that, locally in space, the anisotropy is a smooth function of the scale. Thus, at each location in space, the anisotropy associated with eddies just larger than the grid scale is almost the same as the anisotropy present in the largest eddies on the subgrid scale. Considering the fluctuations produced by our model to be equivalent to the latter, we conclude that we may obtain the anisotropy coefficients by sampling the local structure of the flow just above the grid scale. The flow at this scale is determined by running the large-scale velocity field through a high-pass filter.

It seems reasonable to base the anisotropy coefficients on the root-mean-square values of the local velocity fluctuations. Let the filtered velocity at a point (x_1, x_2, x_3) be given by $\hat{\boldsymbol{u}} = (\hat{u}_1, \hat{u}_2, \hat{u}_3)$, and consider the differences from this velocity at points a distance $\delta = O(h)$ away. In particular, consider the velocity fluctuation

$$\Delta \hat{u}_1 \equiv \hat{u}_1(\boldsymbol{x} + \delta) - \hat{u}_1(\boldsymbol{x}). \tag{21}$$

9

It can be shown that

$$\langle (\Delta \hat{u})^2 \rangle = \tfrac{1}{3} \| \nabla \hat{u}_1 \|^2 \delta^2 + O(\delta^4). \tag{22}$$

It seems reasonable to base the anisotropy coefficients on the root-mean-square values of the local velocity fluctuations. Therefore, using the above estimate, we set

$$s_k = \sqrt{3} \frac{\langle (\Delta \hat{u}_k)^2 \rangle^{\frac{1}{2}}}{\langle (\Delta \hat{u})^2 \rangle^{\frac{1}{2}}} \approx \sqrt{3} \frac{\| \nabla \hat{u}_k \|}{\| \nabla \hat{u} \|}. \tag{23}$$

If the flow is being simulated on a cubical grid, the anisotropy coefficients are completely specified by (23), but such will rarely be the case. Nevertheless, in the case of a potentially anisotropic grid, where the flow is described in terms of generalized coordinates, (23) is still the first step in determining the anisotropy coefficients; in this case, however, the *contravariant* velocities are used, and the derivatives are taken with respect to the transformed coordinates. Also—and this is important—the subgrid-scale velocities produced by the turbulence model in this case are the contravariant velocities.

In order to account for grid-generated as well as physical anisotropies, therefore, we define a normalized vector of anisotropy coefficients, $\boldsymbol{\zeta}$, given by the formula:

$$\boldsymbol{\zeta} \equiv \frac{\boldsymbol{s}\sqrt{3}}{\| \boldsymbol{J}^{-1} \cdot \boldsymbol{s} \|}; \tag{24}$$

where $\boldsymbol{s}$ is defined according to:

$$\boldsymbol{s} \cdot \hat{\boldsymbol{\imath}} \equiv \sqrt{3} \frac{\| \nabla (\hat{\boldsymbol{u}}_c \cdot \hat{\boldsymbol{\imath}}) \|}{\| \nabla \hat{\boldsymbol{u}}_c \|}. \tag{25}$$

In these last two relations, $\boldsymbol{J}^{-1}$ is the inverse of the coordinate transformation Jacobian matrix, $\hat{\boldsymbol{\imath}}$ is a unit vector and $\hat{\boldsymbol{u}}_c$ is the large-scale contravariant velocity vector, filtered to preserve only the smallest (high-wavenumber) components. All norms in the above expressions are 2-norms. The anisotropy vector is normalized such that $\| \boldsymbol{J}^{-1} \cdot \boldsymbol{\zeta} \|^2 = 3$; thus for isotropic turbulence on a cubical grid, $\boldsymbol{\zeta} \cdot \hat{\boldsymbol{\imath}} = 1$.

5.3 Maps

As we have mentioned, the form of the chaotic maps should be related somehow to the statistical properties of real turbulence. In particular, we are interested in the probability density of the velocity fluctuations $\Delta \boldsymbol{u}$. This has been studied by Kailasnath, Sreenivasan, & Stolovitzky [4], in research that was also funded by the AFOSR. Led by Stolovitzky [7] (in work funded by DARPA), these same

10

authors have also examined Kolmogorov's refined similarity hypotheses. The first of these hypotheses takes the form:

$$\Delta u(h) = (h\epsilon_h)^{\frac{1}{3}}V, \tag{26}$$

where ϵ_h is the local average of the energy dissipation rate, over an interval of size h, with $h \ll L$. Under this hypothesis, V is a stochastic variable with a probability density function (PDF) that depends only on the small-scale Reynolds number Re_h (Stolovitzky et al. use a slightly different Reynolds number, $Re_r \cong Re_h^{2/3}$). According to the second refined hypothesis, the PDF of V becomes independent of Re_h, and thus universal, if $Re_h \gg 1$ (or $Re_r \gg 1$). In the inertial subrange, the PDF of V proves to be nearly Gaussian, but slightly skewed, unless the largest scales are excluded, in which case the skewness is zero. Juneja et al.[3] show that the variance $\langle V^2 \rangle$ should be approximately 2, and in fact Stolovitzky et al.[7] found $\langle V^2 \rangle = 1.88$.

Neglecting anisotropy effects, our subgrid-scale model for the velocity generates values

$$u_i \approx (h\epsilon)^{\frac{1}{3}}M \tag{27}$$

(where i indexes the grid position) so there should be a close relation between our stochastic variable M and the stochastic variable V appearing in Kolmogorov's hypothesis. In fact, the velocity increments generated by our model take the form:

$$(u_{i+1} - u_{i-1}) = C(h\epsilon)^{\frac{1}{3}}(M_{i+1} - M_{i-1}), \tag{28}$$

(with $C = O(1)$). The mean square of this is

$$\langle (u_{i+1} - u_{i-1})^2 \rangle = C^2(h\epsilon)^{\frac{2}{3}}\langle M_{i+1}^2 - 2M_{i+1}M_{i-1} + M_{i-1}^2 \rangle, \tag{29}$$

but if M_{i+1} and M_{i-1} are *independent* of each other, the mean square reduces to

$$\langle (u_{i+1} - u_{i-1})^2 \rangle = C^2(h\epsilon)^{\frac{2}{3}}\langle 2M^2 \rangle. \tag{30}$$

Thus the variance of the stochastic variable V should be (approximately) twice the variance of our stochastic variable M, but otherwise the two variables should share the same PDF. In other words, the PDF of the stochastic variable M should be approximately a Gaussian, with unit variance.

Turbulent velocity fields also have the property of intermittent small-scale energy dissipation. Juneja et al.[3] have developed a technique (so far, only in one dimension) for synthesizing velocity fields that have many of the same statistical properties as physical turbulence, including the shape of the PDF for the velocity increments, their variance and skewness, and intermittent dissipation. Their procedure is based on a multifractal construction involving a pair of unequal multipliers, cascaded through several stages. Our procedure for constructing a three-dimensional, time-varying velocity field on the small scale is quite different, but we have suceeded in including most of these statistical properties in our model.
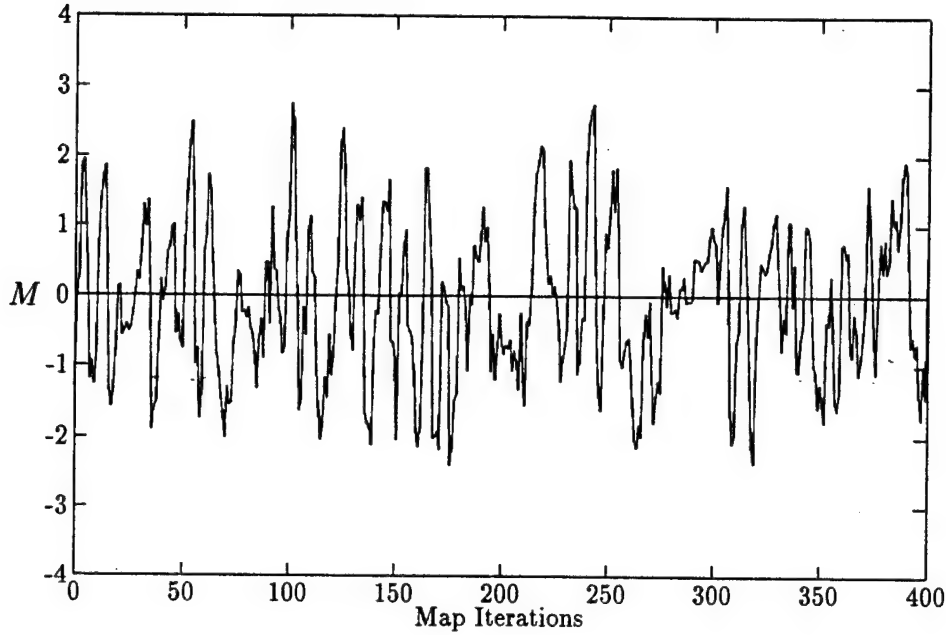
11

Figure 2: Typical time-series for M.

This we have accomplished by constructing our stochastic variable M from the weighted sum of chaotic maps, m_j:

$$M \equiv \sum_j a_j m_j. \tag{31}$$

A total of 2^N maps are used to mimic the intermittent dissipation generated by N stages in the construction of Juneja *et al.*. Currently we are using four maps (a second-stage construction); in this case the appropriate weights a_j are:

$$a_1 = 1.2124, \quad a_2 = 0.7937, \quad a_3 = 0.5196, \quad a_4 = 0.7937. \tag{32}$$

Just *one* of these maps is evaluated at each iteration of the stochastic variable M. At each grid-point we randomly select one of the four maps to begin with, and then start iterating in cyclic sequence. The choice of which map to evaluate at any given iteration could also (and perhaps should) be made randomly, but at the expense of slightly greater arithmetic and complexity, which at present we are not sure is justified. In any case, the procedure appears to work well. For a case corresponding to fully developed turbulence—with the map bifurcation parameter, R (see below) at its maximum magnitude—Figure 2 shows a time-series generated by our stochastic variable M, while Figure 3 shows the corresponding probability density function. The latter quite clearly has the requisite shape and variance.

The elemental chaotic maps m_j are instances of the normalized quadratic map:

$$m_j^{(n+1)} = R2(1 + \sqrt{2})m_j^{(n)} \left[1 - |m_j^{(n)}| \left(1 + \frac{1}{2}(1 + \sqrt{2})\right)\right], \tag{33}$$
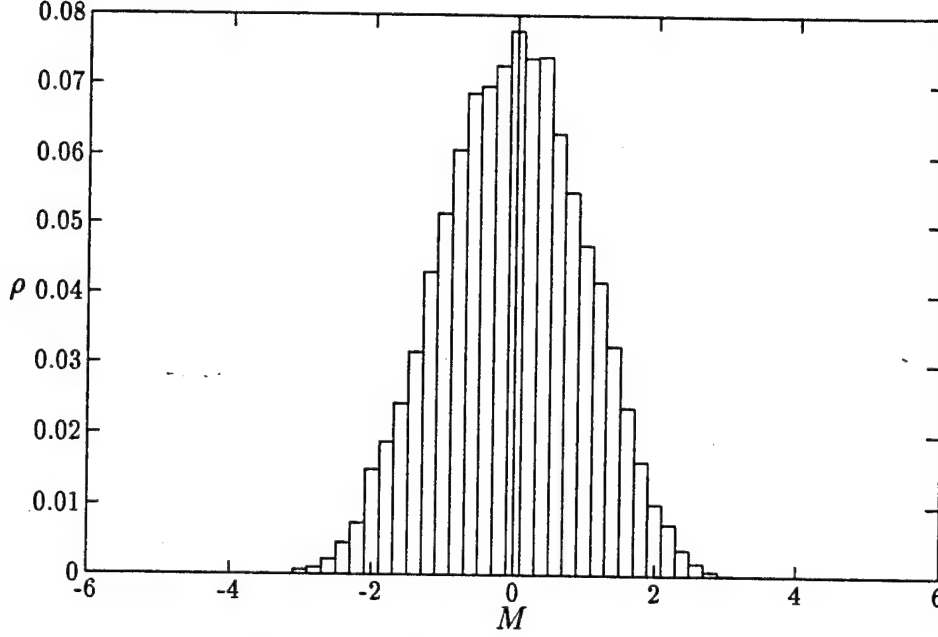
12

Figure 3: Probability density function for M.

or the normalized tent map:

$$m_j^{(n+1)} = \begin{cases} R(-2 - 3m_j^{(n)}) & \text{if } m_j^{(n)} < -\frac{1}{3} \\ R(3m_j^{(n)}) & \text{if } -\frac{1}{3} \leq m_j^{(n)} \leq \frac{1}{3} \\ R(2 - 3m_j^{(n)}) & \text{if } m_j^{(n)} > \frac{1}{3} \end{cases} \tag{34}$$

Here (n) is the iteration number and R is the map's bifurcation parameter (normalized to lie between ± 1).

In order to relate the dynamics of the chaotic maps to the dynamics of the flow, we make the bifurcation parameter R a function of a local large-scale Reynolds number

$$Re_L \equiv \frac{L^2 \|\boldsymbol{\nabla u}\|}{\nu}, \tag{35}$$

where L is a characteristic length for the large-scale motion. This Reynolds number is related to an estimate we have derived for the ratio of the Taylor and Kolmogorov microscales:

$$\frac{\lambda}{\eta} \sim \sqrt{15} Re_L^{\frac{1}{6}}. \tag{36}$$

Although there is not a unique expression relating R and Re_L, the following expression behaves reasonably at the limits and matches certain critical values of the Reynolds number and bifurcation parameter:

$$R = R_{max} \tanh \left[\left(\frac{Re_L}{Re_C} \right)^{\gamma/6} \tanh^{-1} \left(\frac{R_C}{R_{max}} \right) \right]. \tag{37}$$

13

In this expression, Re_C is the critical value of Re_L, R_C and R_{max} are, respectively, the critical and maximum values of the bifurcation parameter R, and γ is a constant used to obtain an appropriate transformation from physical bifurcation parameters to those of the chaotic map. In one of our present studies, these various parameters have been assigned the following values: $Re_C \approx 1430$, $R_C = -0.2071$, $R_{max} = 1$, and $\gamma = 3.6$.

5.4   Velocity Correlations

So far we have said little about the relative independence of the various instances of the stochastic variable, M, used in this model. At present, we are treating the density and energy fluctuations as if they were independent, although they could perhaps be related through the energy equation, or through the equation of state. In fact, we anticipate that it may be desirable to use a different type of chaotic map for each of these quantities, each map being tailored to best match the physical behaviour of the particular quantity being modeled. However, we know from experiment that the three components of the velocity often do not fluctuate independently. This interdependence can be modeled by coupling together the three maps used to generate the velocity fluctuations.

For now, let us consider the correlations between the small-scale velocity components u'_k at a single point in space. These form a tensor:

$$R_{k\ell} \equiv \frac{\langle u'_k u'_\ell \rangle}{\langle u'^2_k \rangle^{\frac{1}{2}} \langle u'^2_\ell \rangle^{\frac{1}{2}}}, \tag{38}$$

where each of the elements has been normalized to lie in $[-1, +1]$. Once again considering velocity fluctuations on a scale just above the grid scale, we estimate

$$R_{k\ell} \approx \frac{(\boldsymbol{\nabla} \hat{u}_k) \cdot (\boldsymbol{\nabla} \hat{u}_\ell)}{\|\boldsymbol{\nabla} \hat{u}_k\| \, \|\boldsymbol{\nabla} \hat{u}_\ell\|}. \tag{39}$$

(As in the section 5.2, these gradients will be evaluated in terms of the filtered contravariant velocities and the transformed coordinates.) The problem is to define a coupling between the stochastic variables for the three velocity components that will reproduce this tensor.

Recall from equation (10) that the subgrid-scale velocity vector $\boldsymbol{w}_S$ (or $\boldsymbol{u}_S$ in the incompressible case) depends on a vector of stochastic variables $\boldsymbol{M}$. Let this latter vector have components $\mathcal{M}_k$:

$$M \equiv [\mathcal{M}_1, \mathcal{M}_2, \mathcal{M}_3]^T. \tag{40}$$

Furthermore, let each of the components $\mathcal{M}_k$ be composed of the weighted sum of three instances of the stochastic variable M:

$$\mathcal{M}_k \equiv \alpha_{k1} M_1 + \alpha_{k2} M_2 + \alpha_{k3} M_3, \tag{41}$$

14

where M_1, M_2, and M_3 are three statistically independent instances of the stochastic variable defined by equation (31); that is

$$\langle M_m M_n \rangle = \begin{cases} \langle M^2 \rangle & \text{if } m = n, \\ 0 & \text{if } m \neq n. \end{cases} \tag{42}$$

And let us normalize the coefficients so that

$$\sum_m \alpha_{km}^2 = 1. \tag{43}$$

Then if the correlation tensor $R_{k\ell}$ is formed from the modelled small-scale velocities, the result is

$$R_{k\ell} = \frac{\langle u_{S_k} u_{S_\ell} \rangle}{\langle u_{S_k}^2 \rangle^{\frac{1}{2}} \langle u_{S_\ell}^2 \rangle^{\frac{1}{2}}} = \sum_\ell \alpha_{km} \alpha_{\ell m}. \tag{44}$$

Equating this with (39) is accomplished straightforwardly by setting

$$\alpha_{km} = \frac{(\nabla \hat{u}_k)_m}{\|\nabla \hat{u}_k\|}. \tag{45}$$

This works because the interaction between the averaging process, the statistical independence of the maps M_m, and the form of (41) mimics the dot product appearing in (39).

Note that, in a turbulent flow, the components of $\nabla \hat{u}$ are likely to fluctuate. Consequently, the coupling coefficients α_{ik} will fluctuate also. Under these circumstances, the coupling coefficients will still contribute to the correlation tensor to the extent that they really are correlated.

5.5 Time-Scale

In order to use our subgrid-scale model in a computational simulation of turbulence, we also must relate the iterations of the stochastic variable to the time-step k used in the simulation, and to a characteristic time for the subgrid-scale eddies. The latter we estimate as a turnover time for a circular eddy of diameter h_k:

$$t_S = \left(\frac{\pi h_k}{|u_k|} \right) f_M, \tag{46}$$

where u_k is the circumferential velocity of the eddy and f_M is a fundamental freqency characteristic of the chaotic maps that make up the stochastic variable M.

Now in the isotropic case,

$$h_k = (3)^{-\frac{1}{2}} h, \tag{47}$$

15

while

$$|u_k| = A_u = C_u u_* Re_h^{\frac{1}{6}}. \tag{48}$$

Therefore, after some manipulation, we derive

$$t_S = \frac{\pi f_M Re_h^{\frac{1}{3}}}{\sqrt{3} C_u \|\nabla u\|}, \tag{49}$$

as an estimate for the subgrid time-scale. This time-scale can also be estimated in terms of the grid-scale vorticity, with results that are comparable in the inertial subrange of turbulence.

The subgrid time-scale t_s proves to be somewhat larger than the time-steps that typically must be used in the numerical simulation of fluid flows. Thus one iteration of the stochastic variable M corresponds to

$$n \approx \frac{t_s}{k} = \frac{\pi f_M Re_h^{\frac{1}{3}}}{k\sqrt{3} C_u \|\nabla u\|} \tag{50}$$

time steps. The singularity that would occur when $\|\nabla u\| = 0$ is not a problem, because the model is turned off when $Re_h < Re_{h\,min} = O(1)$. Practically, under this circumstance, one limits n to being less than some maximum value, and rechecks $\|\nabla u\|$ at each time-step.

5.6 Mass Conservation

For incompressible flows, a final step in the construction of the subgrid-scale velocity field is the removal of the divergence, i.e. the projection of this velocity onto a divergence-free subspace of three-dimensional vector fields. This is justified heuristically on the grounds that the difference between the longitudinal and transverse velocity correlations in a turbulent flow is affected by the divergence-free constraint (see, for example, Batchelor [1]). We have also found that our computational results seem better when we take this step. On this basis we also believe that mass conservation should be imposed on the small-scale field in compressible flow. This remains an area we are actively researching.

5.7 Summary of the Subgrid-Scale Model

In summary, we mimic subgrid-scale turbulence by means of stochastic small-scale fields, each of which is produced by generating, at each point on a grid, a value that is the product of amplitude factors with normalized stochastic variables. The basic amplitude factors are determined in accordance with Kolmogorov's theory of turbulence, although we have been forced to rely on some heuristic arguments in order to estimate the amplitude of the density and energy fluctuations. Our stochastic variables are constructed from a combination of chaotic maps, and

16

their statistics are tailored to match at least the basic statistics of physical turbulence in the inertial subrange. Anisotropy in the velocity field, as well as the cross-correlation of the velocity field components, are introduced as appropriate according to a local sample of the structure of the large-scale velocity field. A time-scale is determined (locally) for the subgrid-scale flow; this time-scale determines in turn how often the stochastic fields are updated. Finally, care is taken to ensure that the subgrid-scale flow is mass-conserving.

6   Implementation for Compressible Flow

The first implementation of the new turbulence modeling scheme for compressible flow began in May 1993. Our goal was to construct the implementation as a relatively simple modification to the existing finite volume compressible flow solver GASP and to test the scheme on a supersonic compression ramp flow. This was carried out, based on the scheme as described in the Mechanical Engineering Department CFD Report by Hylin and McDonough in April 1994. Although the small-scale fluctuations appeared to behave exactly as designed, no large-scale turbulent boundary layer structures appeared in the computed solution. It is crucial to represent such structures in the large-scale solution because they are responsible for the majority of the turbulent transport normal to the wall in boundary layer flows. It is not clear whether our small-scale modeled quantities must actually generate the large-scale structures or merely react to them, but there is strong evidence in the literature that small-scale coherent motions within 100 y^+ units of the wall are responsible for the maintenance of the large-scale outer-region turbulence. We performed numerical experiments in which larger-than-grid-size versions of these near-wall coherent motions were imposed as perturbations to initially laminar supersonic flat plate and compression ramp flows. In both cases, the computed solutions contained large-scale structures of the types observed in physical turbulent flows; this is an example of effective interaction of a large-scale solution and a smaller-scale perturbation, a model for our scheme. We concluded that it is indeed possible to induce large-scale turbulent structures in the large-scale solution, and that for this to occur, the small-scale fields must contain spatially coherent structures.

Based on these conclusions and continuing developments in the derivation of the underlying scheme, an improved implementation is in preparation at present. The new implementation is much simpler to retrofit to existing flow solvers and requires much less computer memory to run than the first implementation. Conservation of mass will be imposed on the small-scale fields, and at least some calculations will include upstream boundary conditions designed to induce the large-scale turbulent structure in the solution.

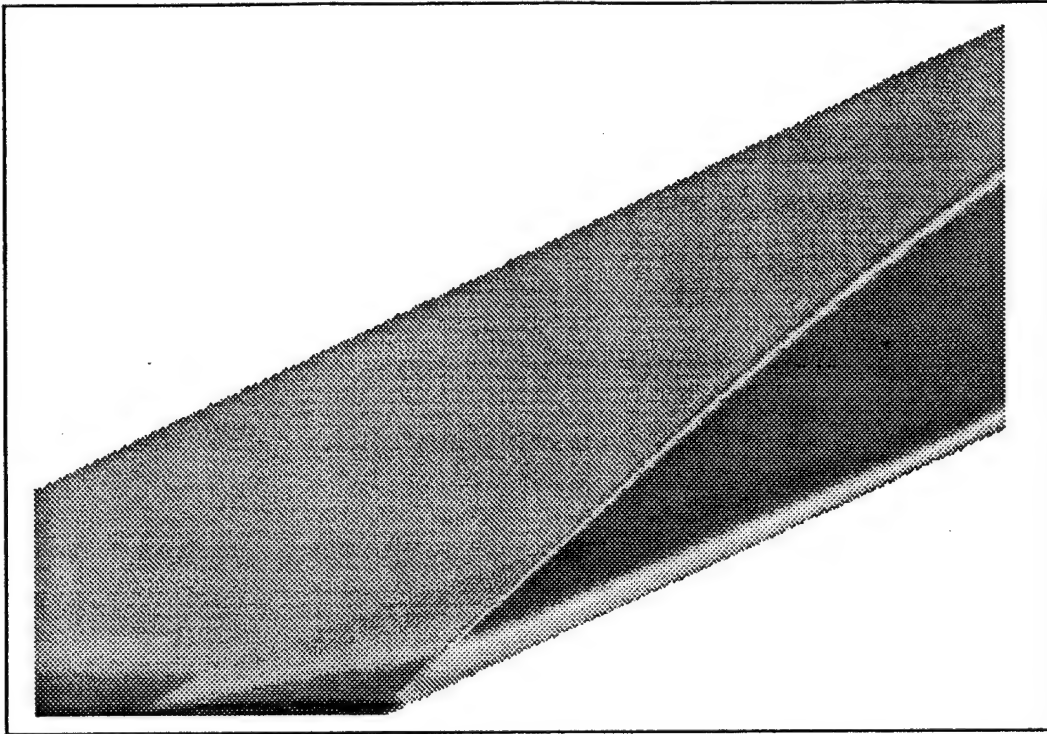In following sections we will describe the work to date.

Figure 4: Instantaneous complete density field.

7   First Implementation

In the first months of this effort, the details of the original modeling scheme were developed and refined at the same time we studied the GASP source code in preparation for incorporation of the new scheme. Based on our initial understanding of the function of the small-scale fluctuations in the method, distinct small-scale variables were assigned to cell centers and cell faces to provide for variation of the small-scale solution across individual cells. We formulated an acceptable method of adapting the Roe flux difference scheme available in GASP to solution of the ATD large-scale equations as they were formulated at the time. This was incorporated into the code. New subroutines to generate the small-scale quantities as well as the auxiliary variables in terms of generalized coordinates were written. We created new code input variables and source code to control the operation of the small-scale model and the production of intermediate visualization output and restart files for large-scale and small-scale variables.

The new scheme was tested on a 2-D compression ramp flow. The corresponding physical experiments were conducted at Princeton. The geometry is a 24° ramp in a Mach 2.85 flow at a Reynolds number of 1.6×10^6/in. The calculations were carried out on a 240×80 grid that was highly stretched in the wall-normal direction. For purposes of reference in the following figures, the ramp corner is located at cell 89 in the streamwise direction. Figure 4 shows an instantaneous complete density field during the calculation; this shows the main shock structures
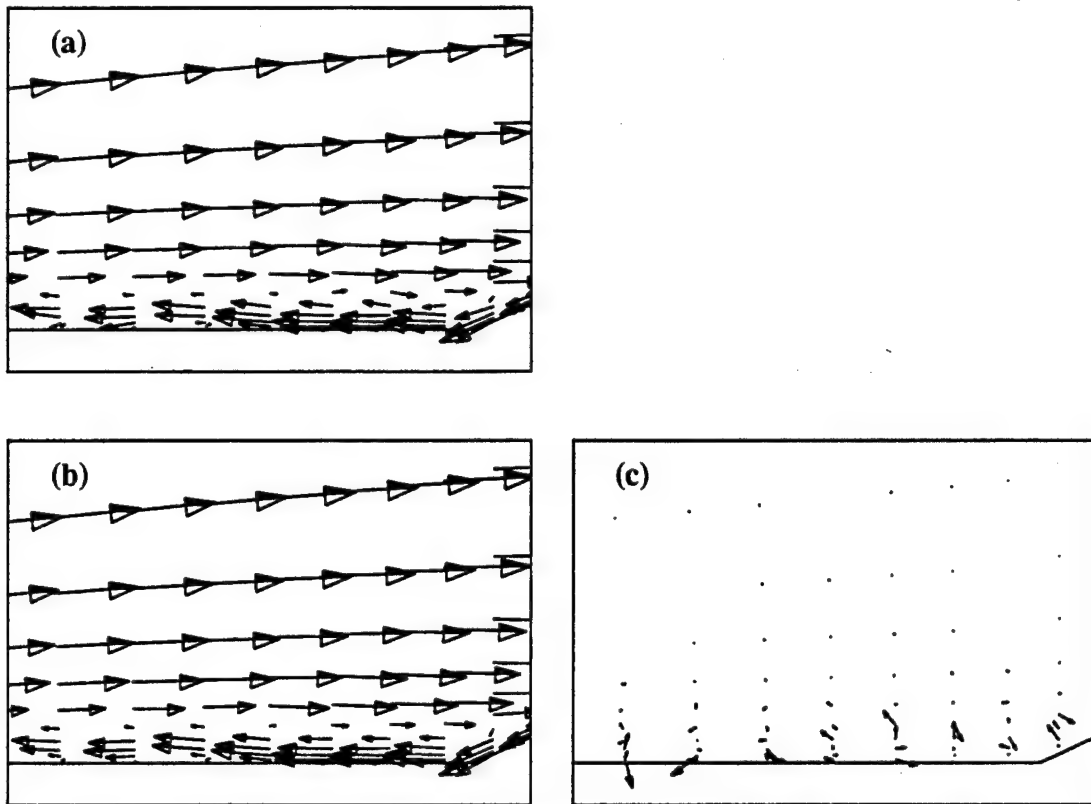
18

Figure 5: Instantaneous velocity fields in compression corner; (a), complete velocity; (b), large-scale velocity; (c), small-scale velocity.

and the recirculation region. The shock structure fluctuates in the streamwise direction in the experiments, but no such motion was evident in our calculations.

The small-scale fluctuations behaved as designed, with appropriate dynamics and amplitudes determined by local large-scale conditions.

Figure 5 shows a close-up view of the compression corner, with every fifth velocity vector in the complete, large-scale, and small-scale velocity fields; the recirculation region is evident in (a), the complete velocity field. Although it is not obvious, somewhat less grid-scale oscillations are present in the large-scale field (b) than in the complete field. Panel (c) shows the corresponding small-scale velocity field and its contribution to the complete field. The vectors in this panel have been scaled up by a factor of about two from that used in the other panels to make them more visible. For the small-scale field, notice that the largest amplitude fluctuations are located close to the wall where the shear is highest. This feature is built into the model for the velocity fluctuations. Figure 6 illustrates this again; in the figure, the vectors have been scaled up by a factor of five from the previous figure to make them more visible. Note that the modeled small-scale velocity fluctuations are essentially nonexistent in the freestream regions on the flow field as they should be.

The next figure shows line plots of instantaneous complete primitive variable
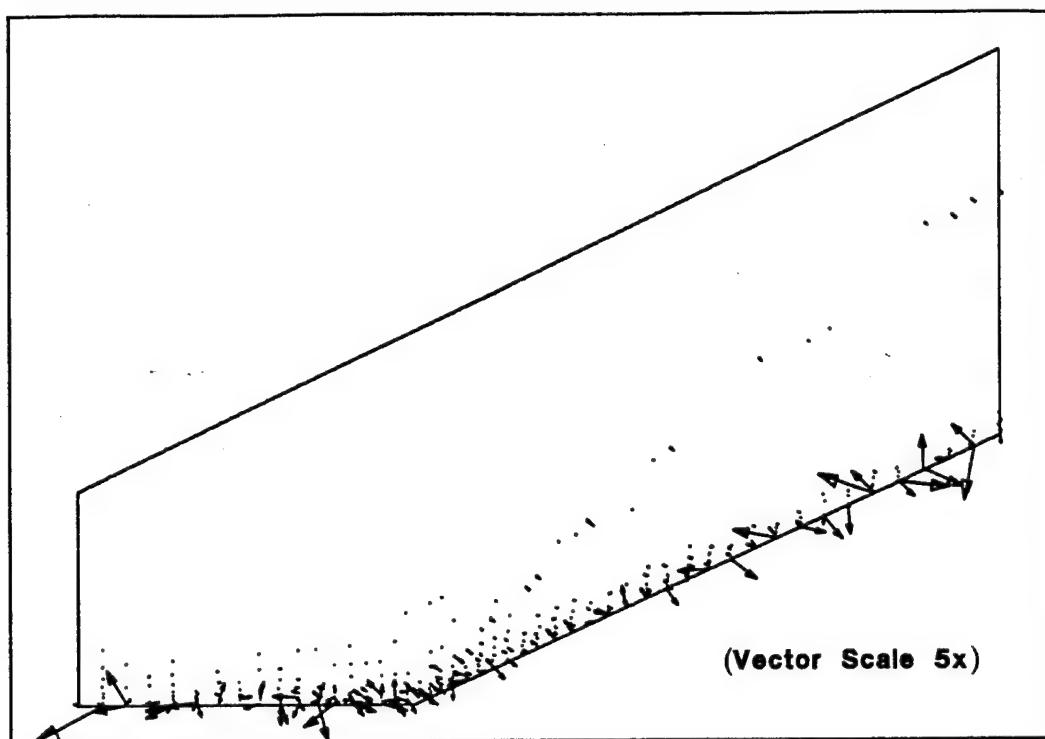
Figure 6: Instantaneous small-scale velocity field (scaled 10x), full domain.

quantities along a streamwise line located at the fifth cell from the wall. The fluctuation amplitudes vary widely along the domain, but they are of reasonable size in comparison with local complete values. The evident spatial chaos is accompanied by temporal chaos, although no time series are presented here.

Results from these calculations were presented at meetings of the American Physical Society Division of Fluid Dynamics in Albuquerque, NM, in November 1993, and in Atlanta, GA, in November 1994.

8 Induction of Large-Scale Turbulent Boundary Layer Structure

As promising as the model behavior was in the ramp calculations, the interaction of the fluctuations with the large-scale solution was less than satisfactory. No large-scale coherent boundary layer structures appeared in the time-dependent ATD solution. This was considered a serious defect since such structures are responsible for the majority of the turbulent transport and they are the main features to be computed in the large-scale solution. No statistics were computed for the 2-D ramp flowfield because the absence of large-scale motion in the field removes any hope of a reasonable comparison with experiment.

Attention focussed on how to ensure proper interaction of the small-scale quantities with the large-scale solution in the context of a finite volume scheme. The
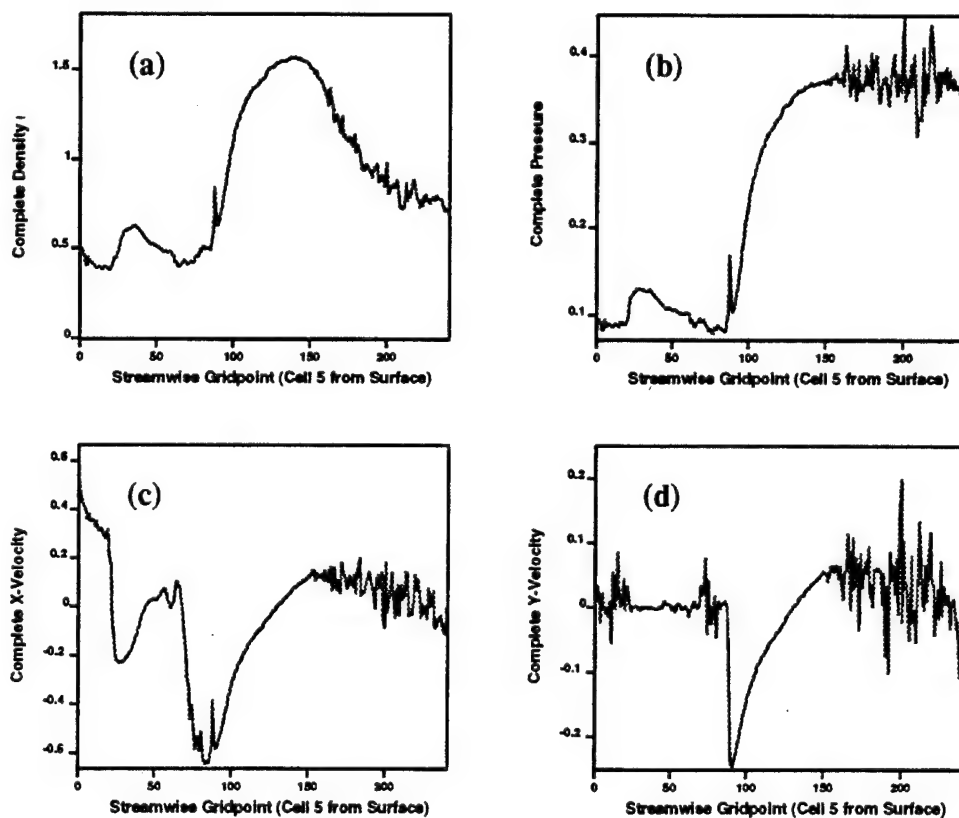
Figure 7: Instantaneous complete variable fields along a streamwise line five cells from the surface; (a), density; (b), pressure; (c), x-velocity; (d), y-velocity.

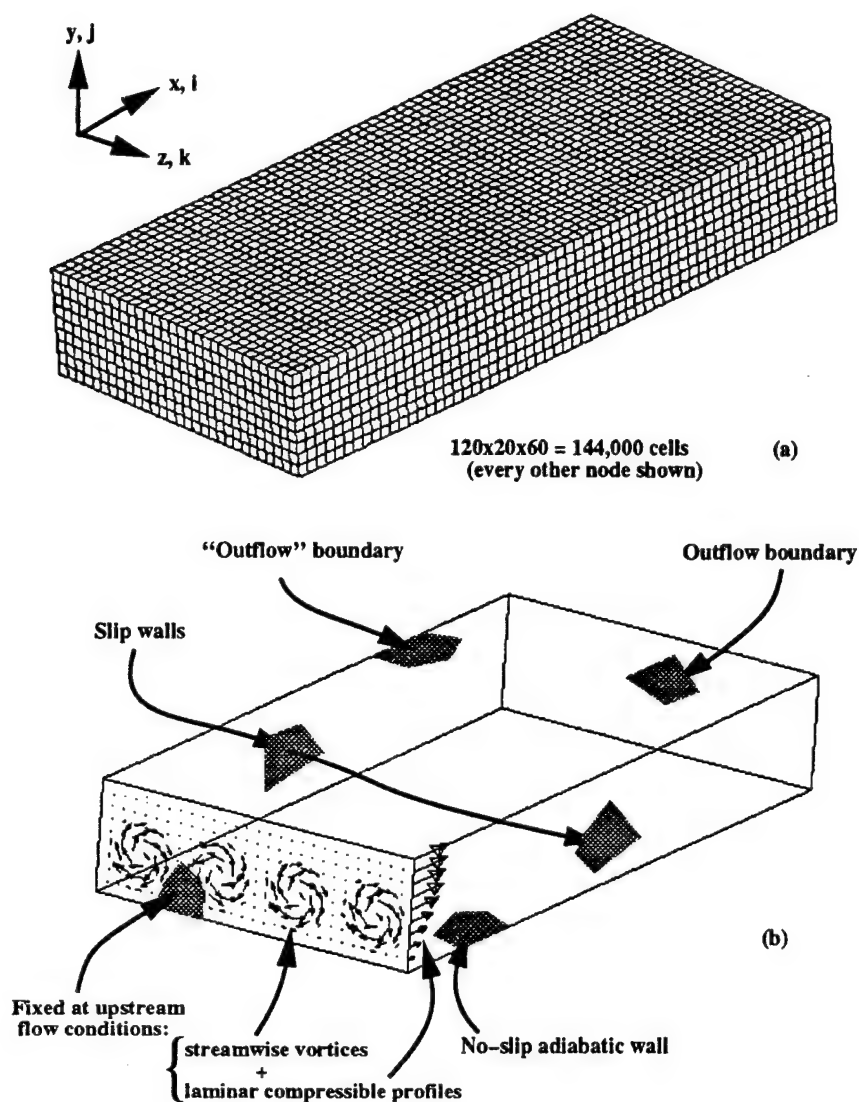120x20x60 = 144,000 cells   (a)
(every other node shown)

Figure 8: (a), grid; (b), boundary conditions.

consensus of the coherent structure literature and recent developments in stability theory is that interaction of quasi-streamwise vortices and streaks in the inner near-wall layer are likely responsible for initiating and maintaining wall-bounded turbulence, and in particular, this interaction directly produces the large-scale structures that we must compute. We carried out 3-D computations of a supersonic flat plate boundary layer under the same flow conditions used in the ramp calculation.

The computational grid contained $120 \times 60 \times 20$ cells. As shown in Figure 8, the laminar flow initial condition was perturbed by streamwise vortices imposed as a stand-in for the small-scale quantities we seek to model. No turbulence model was employed in the calculation. The experiments showed that such a computed boundary layer is indeed susceptible to "transition" under the influence of

the streak-vortex interaction mechanism. The large-scale coherent structures in the solution were quite similar in character to those observed in fluid turbulence. Figure 9(a), a contour plot of streamwise momentum at the first cell center off the plate surface (plane j=1), thresholded to highlight values less than 20% of the freestream value, shows the streaky structures described as essentially ubiquitous in the sublayer and buffer regions of all turbulent boundary layers. These structures occur at very small length scales near the wall in physical flows, but they appear at scales larger than the grid size in the calculation. Figure 9(b) is a plot of wall-pressure contours, limited to those greater than the initial freestream pressure. The form of these contours corresponds to literature descriptions of the high wall-pressure regions as relatively rounded spots rather than elongated regions.

Figure 10 shows contours of spanwise vorticity in the wall-normal plane on the domain spanwise centerline. The four parts of the figure are from successive times in the flow evolution. The most noticeable feature of this sequence is the development and convection downstream of a large bulge in the rotational-irrotational interface, and an accompanying incursion of irrotational fluid toward the wall. This is a common feature often observed in turbulent boundary layers. The convection speed of the bulge can be estimated from this sequence to be about 80% of the freestream velocity; this is consistent with values found in incompressible low-Reynolds number boundary layers, but is lower than the corresponding percentage for boundary layers at this Mach number, which has been measured to be about 90%. In the figure we also observe sloping regions of very high shear near the wall. These shear layers also agree well with experimental observations.

Figure 11(a) is similar to Figure 10(c); it shows spanwise vorticity, with features evident as before. We call attention to some details here. Figure 11(b) shows velocity vectors in the plane. The profiles at any given downstream station bear little resemblance to the nearly undisturbed profiles at the upstream boundary at left. In the downstream third of the domain, we find a structure with a sharply-defined sloping upstream interface that appears to be almost a discontinuity in the streamwise velocity. The structure extends all the way across the boundary layer. Regions of both high- and low-speed fluid exist within this structure, with a range of scales present. This corresponds to the feature noted by many to be the most readily detected in experiments, the sloping δ-scale "backs" of large bulges. The fluid ahead of such backs is frequently observed to rotate slowly in a direction consistent with its downstream motion. In Figure 11(c) we plot the same velocity vector field, but here in a reference frame moving at the previously estimated convection velocity of the structure. The field does in fact show slow rotation as if rolling downstream along the plate. Further, at two locations along the upstream side of these structures, high-speed fluid from upstream encounters low-speed fluid with the consequence of very high local pressure. This is illustrated for this plane in Figure 11(d), which shows contours of pressure. The two dark regions in the plot about halfway up in the domain are the areas in question.

Figure 12(a) shows cross-stream sections at the five streamwise stations marked in Figure 11. Figure 12(b) is a cross-stream section of the entire domain at $x = 3.5$
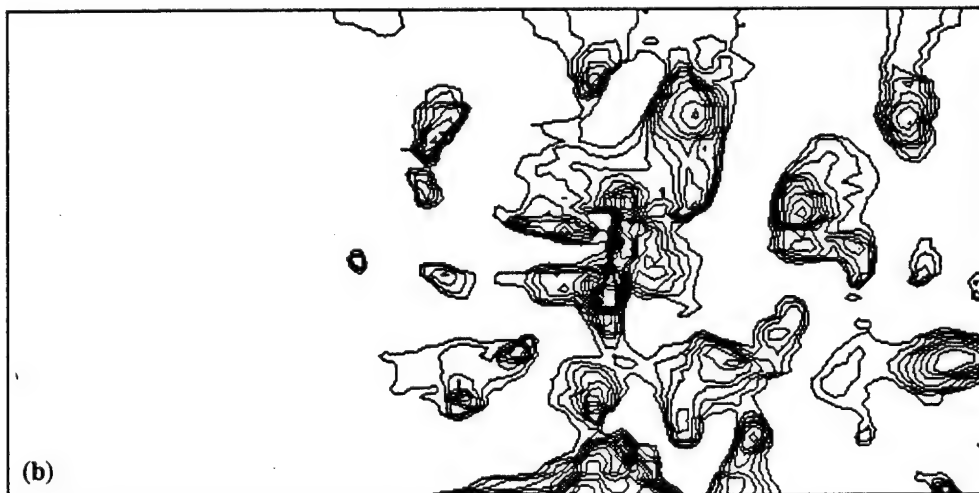
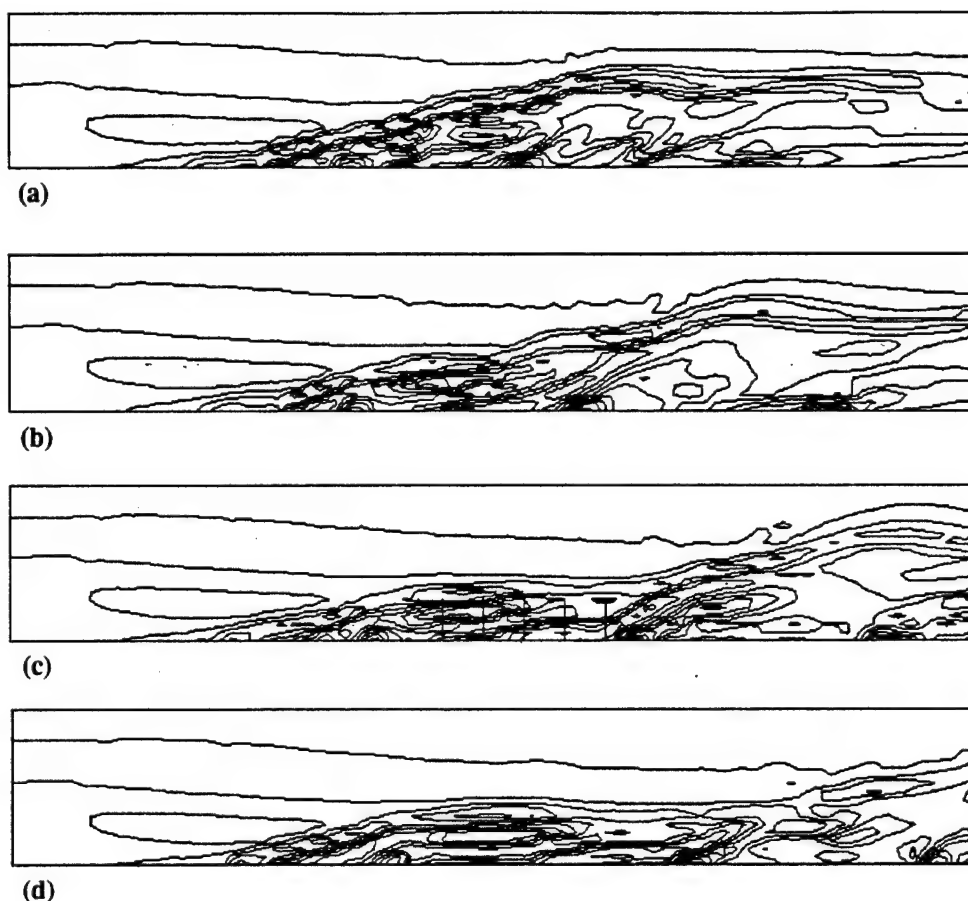Figure 9: Wall contours at t = 0.50 msec: (a), low streamwise momentum; (b), high pressure.

Figure 10: Contours of spanwise vorticity at time = (a), 0.40 msec; (b), 0.45 msec; (c), 0.50 msec; (d), 0.55 msec.

in, showing contours of pressure and projections of the velocity vectors onto this plane. The initial streamwise vortices are still very much in evidence, but smaller scale motions have also developed. Note that the pressure contours in this plane show the existence of low-pressure cores in the vortices; the low-pressure cores have been observed to be a reliable and convenient indicator of vortical structures in complex flowfields. Vortical structures are connected in some way to each of the other classes of motion; in the viscous sublayer and buffer layer, quasi-streamwise vortices are observed to play a central role, although the precise dynamics have not yet been established. In the sections of Figure 12(a) we see just such a vortical structure. The sections show velocity vectors projected onto the cross-stream plane, with pressure contours superimposed. In each section we see flow circulating around a core of low pressure. The vortex core is located within two or three grid cells of the wall in the upstream section at left. The core rises going downstream, in accordance with the observation that quasi-streamwise vortices are quite small and nearly horizontal near the wall, but their diameter and inclination increase downstream, until in the mid-ranges of the layer, the inclination angle
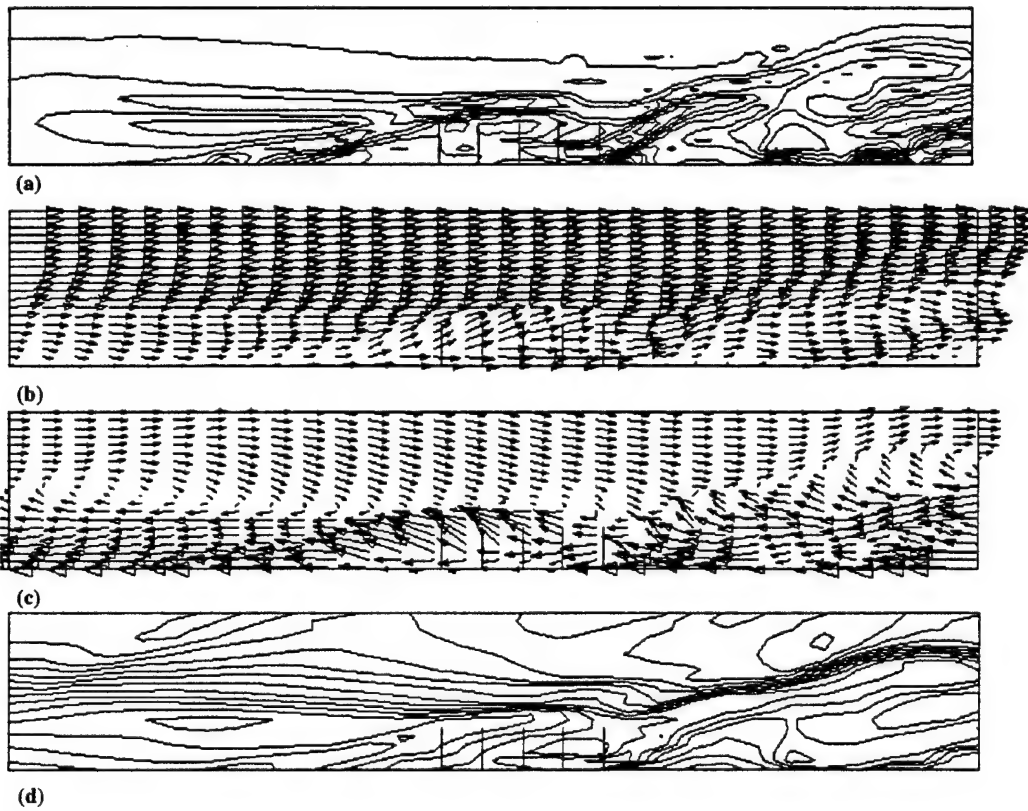
25

Figure 11: Time = 0.50 msec; (a), spanwise vorticity contours; (b), velocity vectors; (c), velocity vectors in reference frame convecting at 80% U_∞; (d), pressure contours.
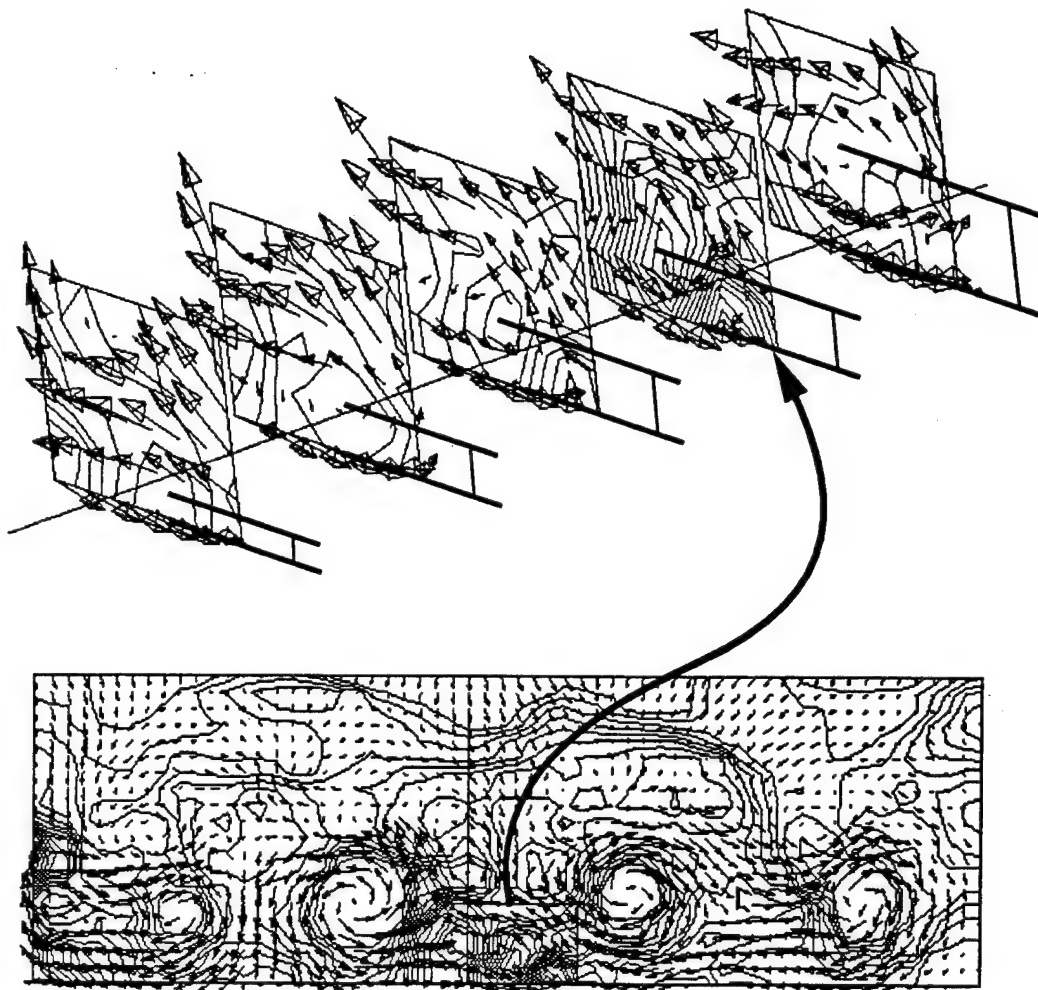
Figure 12: Time 0.50 msec; (a), sections through streamwise vortex at five stream-wise stations; cross-stream velocity vectors and pressure contours; (b), cross-stream velocity vectors and pressure contours at streamwise station x = 3.5 in.

27

averages about 45°-60°.

The flowfield appears to have some structural features that occur within the viscous sublayer and buffer layer. These structures appear at scales much larger than those expected in the physical flow. The presence of these structures in our computed solution is consistent with conjectures about the importance of interaction of vortices and streaks in physical wall-bounded turbulence. Such an interaction will likely be necessary in the large-scale computed solution for large-scale 'turbulent' motion to be maintained, unless the modeled turbulent sub-grid fluctuations can be made to carry out this function in some way.

On the other hand, the coherent structures that typically occur at δ-scale, such as the large bulges and the sloping "backs", were well-represented in size and speed of propagation. This suggests that we may hope to compute such structures, our ultimate goal, in the future with an appropriate numerical scheme.

The turbulent structures in this computed solution were provoked by the presence of perturbations in the form of streamwise vortices. We infer that if the modeled small-scale variable fields, which function similarly to these perturbations in our turbulence modeling scheme, contain some component of such motion, that a similar transition effect may occur. This is one of the bases for our belief that coherent structure will be necessary in the small-scale fields for effective interaction with the large-scale solution.

The results of these experiments were reported in more detail in an AIAA Paper presented at the 34th AIAA Aerospace Sciences Meeting, Reno, NV, in January 1996.

A similar experiment was carried out for the 3-D compression ramp flow that was used as our first test case. In this calculation, the computational grid contained $160 \times 50 \times 20$ cells. As in the previous experiment, streamwise vortex perturbations were superimposed on the laminar supersonic initial condition and the flow was evolved without a turbulence model. Turbulent structure developed quickly and did not seem to diminish as the calculation proceeded, in contrast with the flat plate case. Activity downstream of the recirculation shock was particularly dramatic. Animation of the solution revealed time-dependent shock structures that compared well with the visual observations of experimentalists. A typical field is presented in Figure 13; the figure shows filled density contours at an instant about half a millisecond (physical time) into the calculation. The large-scale vortical structures rolling up in the boundary layer downstream of the recirculation shock are filled with low-speed fluid that produces secondary shocks as high-speed fluid strikes them from behind. One highly unsatisfactory aspect of the computed solution was that the recirculation shock moved upstream during the calculation until it almost reached the inflow boundary. The more or less final location of this shock was very far from that measured in the Princeton lab.

The results of this calculation were reported at the 48th Annual Meeting of the American Physical Society Division of Fluid Dynamics, Irvine, CA, in November 1995.

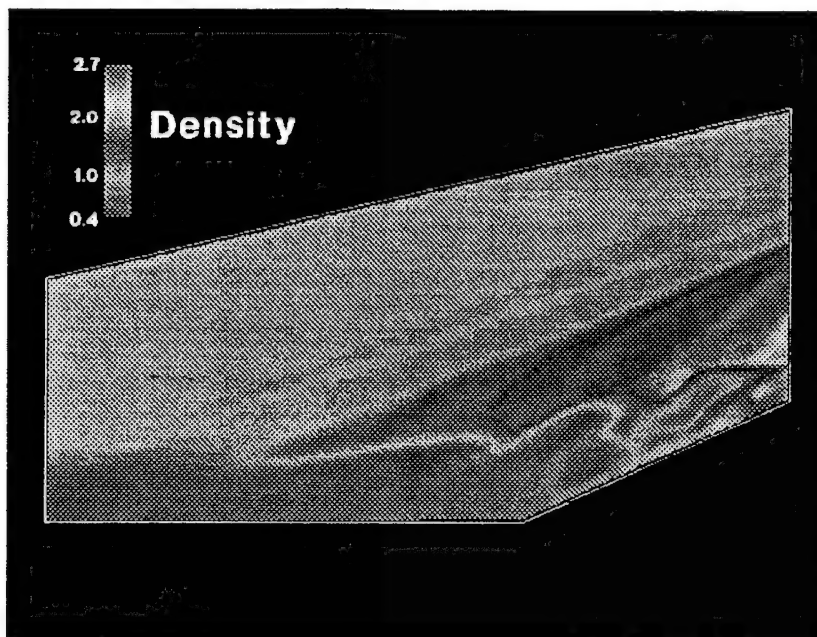The results of this calculation were presented at

Figure 13: Instantaneous density field, 24° compression ramp.

9   Revised Implementation

At present, revisions to the formulation and implementation of the turbulence modeling scheme are in progress. The underlying formulation of the decomposed equations has been reconsidered. The formulation for the large-scale equations now requires construction of the large-scale part of the advective terms in the governing equations, with an approximation to the complete solution used in this process. This removes the question of how to split the various scale interaction terms among the several sets of decomposed equations and avoids the accompanying theoretical difficulties of deriving characteristic-based solution schemes with rigor. From the practical point of view, it also greatly simplifies implementation; the numerical methods in the existing flow solver can be used for the new formulation without modification except that the large-scale and small-scale quantities must be combined to produce approximate complete quantities at the beginning of each time step.

Our computed compressible flow experiments with streamwise vortex perturbations and our experience with calculating incompressible flow over a backward-facing step lead us to believe that effective interaction between the modeled small-scale quantities and the computed large-scale solution occurs when the small-scale field contains structures at scales larger than the grid scale. This implies that it is not necessary to maintain small-scale variables at cell centers *and* cell faces as we have done previously, because variation across individual cells has little effect on the large-scale solution. In addition, use of small-scale variables at several locations per cell greatly increases the memory requirements over the original flow

29

solver. Therefore, in the new implementation, small-scale variables are carried only at cell centers, the nominal locations for the large-scale variables.

Our concern with effective scale interaction will also affect our imposition of the continuity equation on the modeled small-scale field. We will prefer a method that automatically produces coherent structure in the small-scale velocity field itself at each time step, in the same manner as in the incompressible case.

Experiments with the reformulated scheme will be reported in future publications.

Papers and Presentations

The following papers and presentations have resulted from this work.

Refereed Conference Papers

McDonough, J. M., Yang Y. and Hylin, E. C., "Modeling Time-Dependent Turbulent Flow over a Backward-Facing Step via Additive Turbulent Decomposition and Chaotic Map Models," in Proc. 1st Asia CFD Conf., Hui *et al.*(eds.), Hong Kong Univ. Sci. Tech., Vol. 2, pp 747– , 1995.

Weatherly, D. C. and McDonough, J. M., "Computed Large-Scale Compressible Boundary Layer Structure Stimulated by Vortical Perturbations," presented at AIAA 34th Aerospace Sciences Meeting, Reno, Jan. 15–18, 1996.

Conference Presentations

Hylin, E. C., Weatherly, D. C., and McDonough, J. M., "Modeling the Subgrid-Scale Flow with a Chaotic Map," presented at Amer. Phys. Soc. 46th Ann. Mtg. Division of Fluid Dynamics, Albuquerque, NM, Nov. 21–23, 1993.

Weatherly, D. C., Hylin, E. C. and McDonough, J. M., "Additive Turbulent Decomposition with Chaotic Map Subgrid-Scale Model for Compressible Flow," presented at Amer. Phys. Soc. 46th Ann. Mtg. Division of Fluid Dynamics, Albuquerque, NM, Nov. 21–23, 1993.

McDonough, J. M., Zhong, X. and Hylin, E. C., "Additive Decomposition of the Navier–Stokes Equations with Chaotic Map Subgrid Models: Application to Intermittent Pipe Flow," presented at Amer. Phys. Soc. 47th Ann. Mtg. Division of Fluid Dynamics, Atlanta, GA, Nov. 20–22, 1994.

Weatherly, D. C., Hylin, E. C. and McDonough, J. M., "Additive Turbulent Decomposition of the Navier–Stokes Equations with Chaotic Map Subgrid Models: Application to Supersonic Ramp Flow," presented at Amer. Phys. Soc. 47th Ann. Mtg. Division of Fluid Dynamics, Atlanta, GA, Nov. 20–22, 1994.

McDonough, J. M., Yang, Y. and Hylin, E. C., "Incompressible Flow over a Backward-Facing Step," presented at Amer. Phys. Soc. 48th Ann. Mtg. Division of Fluid Dynamics, Irvine, CA, Nov. 19–21, 1995.

Weatherly, D. C., Hylin, E. C. and McDonough, J. M., "Supersonic Compression Ramp Calculations with Dependent-Variable Sub-grid Models," presented at Amer. Phys. Soc. 48th Ann. Mtg. Division of Fluid Dynamics, Irvine, CA, Nov. 19–21, 1995.

Invited Talks and Lectures

McDonough, J. M., "The Additive Turbulent Decomposition Formalism: An Alternative Approach to Turbulence Modeling and Simulation," presented at Hong Kong Univ. Sci. Tech., Clear Water Bay, Hong Kong, May 24, 1994.

_____ , "Additive Turbulent Decomposition of the Navier–Stokes Equations: An Alternative Formalism for Turbulence Modeling," presented at UCLA Mechanical, Aerospace & Nuclear Engineering Seminar, Mar. 23, 1995.

_____ , "Turbulence Computations Based on Unaveraged Equations and Non-linear Chaotic Map Subgrid-Scale Models," presented at NASA Lewis Research Center, Heat Transfer Branch, Aug. 22, 1995.

_____ , "Small-Scale Turbulence Modeling and Simulation via Additive Turbulence Decompositions of the Navier–Stokes Equations," presented at the Institute for Mathematics and its Applications, Univ. of Minnesota, Oct. 26, 1995.

References

[1] G. K. Batchelor, *The Theory of Homogeneous Turbulence*, Cambridge University Press, 1953.

[2] E. C. Hylin and J. M. McDonough, *Chaotic map models for the small-scale quantities in an additive decomposition of the Navier–Stokes equations. Part 1. Theory*, Tech. Report CFD–01–94, Department of Mechanical Engineering, University of Kentucky, 1994.

[3] A. Juneja, D. P. Lathrop, K. R. Sreenivasan, and G. Stolovitsky, *Synthetic turbulence*, Physical Review E **49** (1994), no. 6, 5179–5194.

[4] P. Kailasnath, K. R. Sreenivasan, and G. Stolovitsky, *Probability density of velocity increments in turbulent flows*, Physical Review Letters **68** (1992), no. 18, 2766–2769.

[5] S. Kida and S. A. Orszag, *Energy and spectral dynamics in forced compressible turbulence*, Journal of Scientific Computing **5** (1990), no. 2, 85–125.

[6] A. N. Kolmogorov, *Dissipation of energy in the locally isotropic turbulence*, Dokl. Akad. Nauk. SSSR **32** (1941), no. 1, Reprinted, in English translation, in Proceedings of the Royal Society of London A (1991) **434**: 15–17.

[7] G. Stolovitzky, P. Kailasnath, and K. R. Sreenivasan, *Kolmogorov's refined similarity hypotheses*, Physical Review Letters **69** (1992), no. 8, 1178–1181.